JOURNAL OF CATALYSIS 94, 79–96 (1985)

Electron Microscopy Studies Relating to Methanol Oxidation over Ferric Molybdate and Molybdenum Trioxide Catalysts

P. L. GAI* AND P. A. LABUN†

Department of Metallurgy and Science of Materials, University of Oxford, Parks Road, Oxford OX1 3PH, United Kingdom; and †Department of Metallurgy and Materials Science, Case Western Reserve University, Cleveland, Ohio 44106

Received February 27, 1984; revised February 18, 1985

Microstructural characterization of ferric molybdate and molybdenum trioxide catalysts used for the oxidation of methanol to formaldehyde has been carried out by *in situ* electron microscopy and state-of-the-art high-resolution electron microscopy and electron diffraction techniques. Microanalytical techniques have also been used for detailed investigation of the fresh and aged catalysts. The observations on ferric molybdates have shown that under *in situ* reaction conditions using CH_3OH (MeOH), MeOH-O_2, as well as H_2 environments, reduction of the catalyst proceeds via two or possibly three reaction routes *simultaneously*. Reduction, however, is limited in the presence of gaseous oxygen. In MoO_3, *in situ* experiments under MeOH and also H_2/He environments have shown that a variety of extended defects are generated. The changes in the catalyst microstructure in the environment of methanol, oxygen, and hydrogen under operating conditions are characterized and compared.

INTRODUCTION

Formaldehyde is produced commercially from methanol using a mixture of ferric molybdate and molybdenum trioxide as catalyst (*1–3*). The process involves methanol and air mixtures and formaldehyde is formed by the selective oxidation of methanol over mixed Fe–Mo oxides at operating temperatures of ~300–400°C. High activity, selectivity, stability, and long life make the system one of the important industrial catalysts available for methanol oxidation. However, the activity and selectivity of the microcrystalline catalysts are critically dependent upon the microstructural changes (at nanometric size level) under operating conditions. Despite detailed solid-state chemical work, e.g., Refs. (*4, 5*), the microstructural changes (which often occur at the submicrometer level) are not fully understood because the conventional techniques (e.g., X-ray and neutron diffraction) cannot provide accurate information at this size level. Electron microscopy techniques, on the other hand, are ideally suited and are being increasingly used for microstructural characterization. *In situ* electron microscopy (EM) is used to examine the catalysts directly under operating conditions. Solid-state changes as a function of gaseous environments and temperature, together with nucleation of defect structures, unstable phases, catalyst deactivation, and reoxidation, can be examined with this technique. Such studies, together with parallel chemical experiments (in a gas chromatograph/mass spectrometer (GC–MS) system) and detailed microchemical and high-resolution electron microscopy (with a point resolution of 1.7 Å) allow one to correlate microstructure with activity and selectivity and to determine optimum conditions for better catalyst performance.

EXPERIMENTAL

(*a*) *Catalyst preparation.* Iron molybdates were prepared by precipitating ammonium molybdate and ferric chloride solutions (*1, 2*). The precipitate was calcined at 400–500°C and dried at higher temperatures in air for several days to obtain the pure $Fe_2Mo_3O_{12}$ phase as was con-

0021-9517/85 $3.00

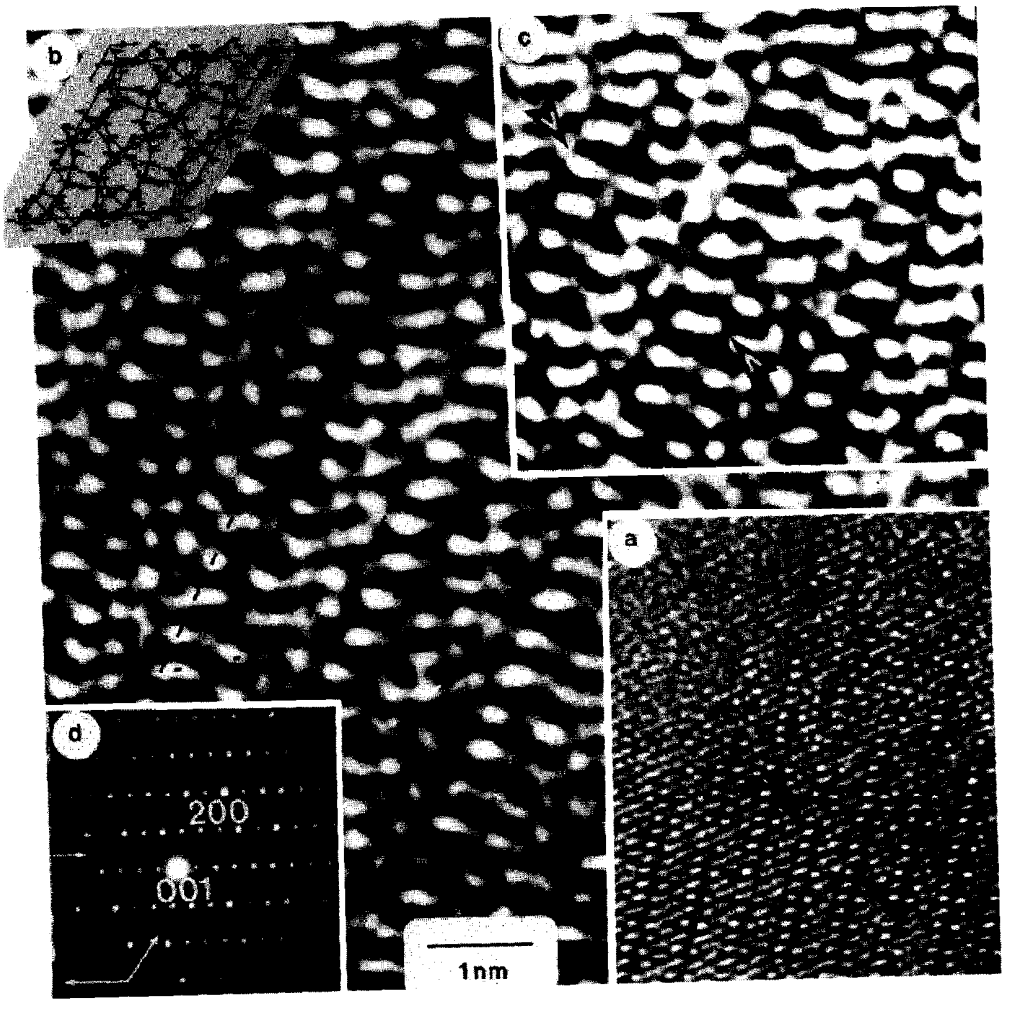
b
c
a
d
200
001
1nm

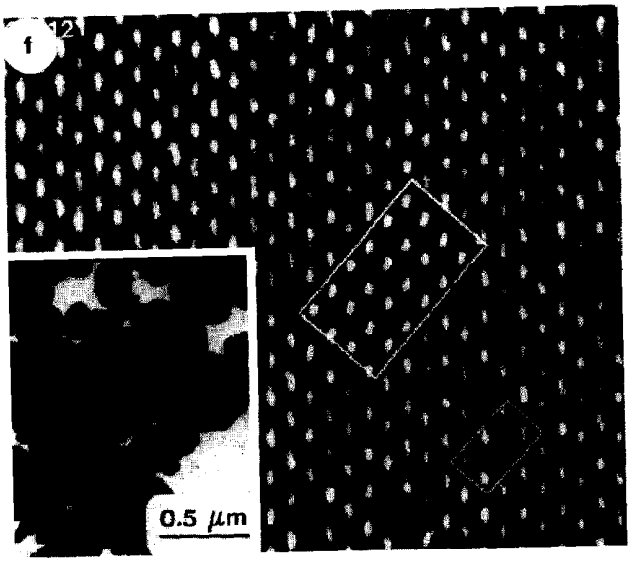
f
0.5 μm

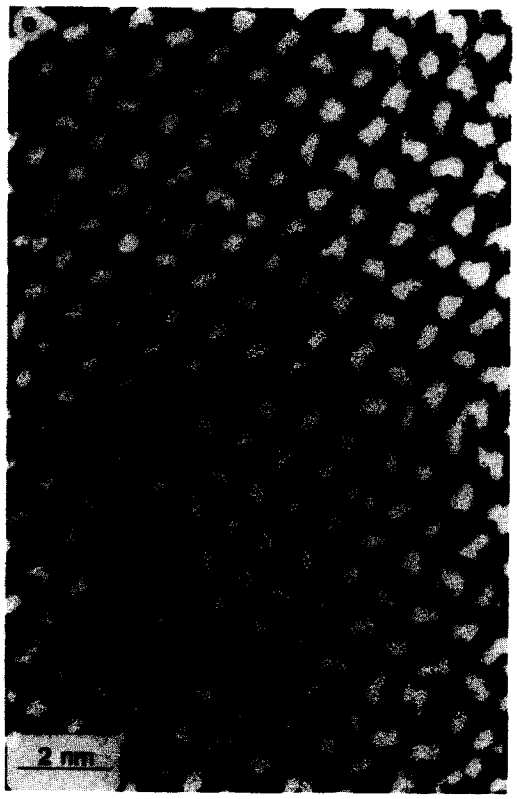

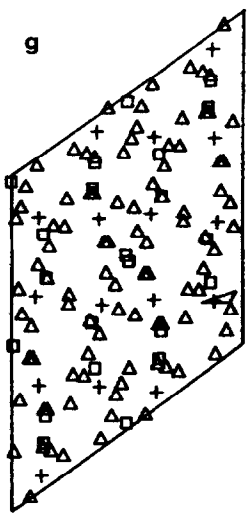

FIG. 1. High-resolution lattice images of $Fe_2Mo_3O_{12}$. (a) (010) Experimental image with amorphous region near (a); (b) and (c) are digitally processed images of (a); (d) (010) electron diffraction pattern with arrows indicating row of faint reflections; (e) (101) lattice image with computed image inset; (f) (121) image with morphology of the fresh sample inset; (g) atomic projection of $Fe_2Mo_3O_{12}$ in (010): (+) Fe; (□) Mo; (△) O.

firmed by X-ray diffraction. MoO_3 crystals were obtained by vapor-phase transport (*6*) and as-grown single crystals were used in the experiments, following pretreatment in oxygen.

(*b*) *Electron microscopy.* The dynamic experiments were carried out in a gas reaction cell with a single-tilt hot stage (*7*) fitted to an AEI-EM7 high-voltage electron microscope (HVEM), capable of operating with realistic gas pressures (up to 1 atm) and temperatures (up to ~1000°C). The dynamic events were recorded continuously using *low* beam currents on a video system coupled to a low-light level TV camera and also on photographic films. "Blank" experiments (without the beam, to reduce radiation damage if any) were also performed in each case to confirm *in situ* observations of microstructural changes: in this case, the electron beam was turned off while heating the sample and turned on only for a few seconds at a time to record the images. Reduction experiments were carried out *in situ* on crystallites of $Fe_2Mo_3O_{12}$ powder and of MoO_3, in continuous flows of H_2 gas initially (to simplify defect analysis) and later, CH_3OH–He mixture. In the latter case, helium gas was bubbled through methanol and a mixture of a few Torr of methanol (MeOH) vapor with He was allowed into the gas reaction cell. Reactions were also carried out in MeOH–O_2 mixtures. Some of the crystal tilting experiments to obtain crystallographic zones were carried out at room temperature using a double-tilt (±25°) environmental stage. Parallel experiments were carried out on larger amounts (0.5–2 g) of similar samples in a fixed-bed microreactor fitted to a gas chromatograph (Varian 3700)–mass spectrometer (VG) system (GC–MS) controlled by an Apple microcomputer. The samples were examined by electron microscopy to confirm the direct studies.

The microstructural characterization was complemented by HREM using a JEOL JEM 200CX EM (*8*) operated at 200 keV (with a point resolution of ~1.7 Å) and cou-

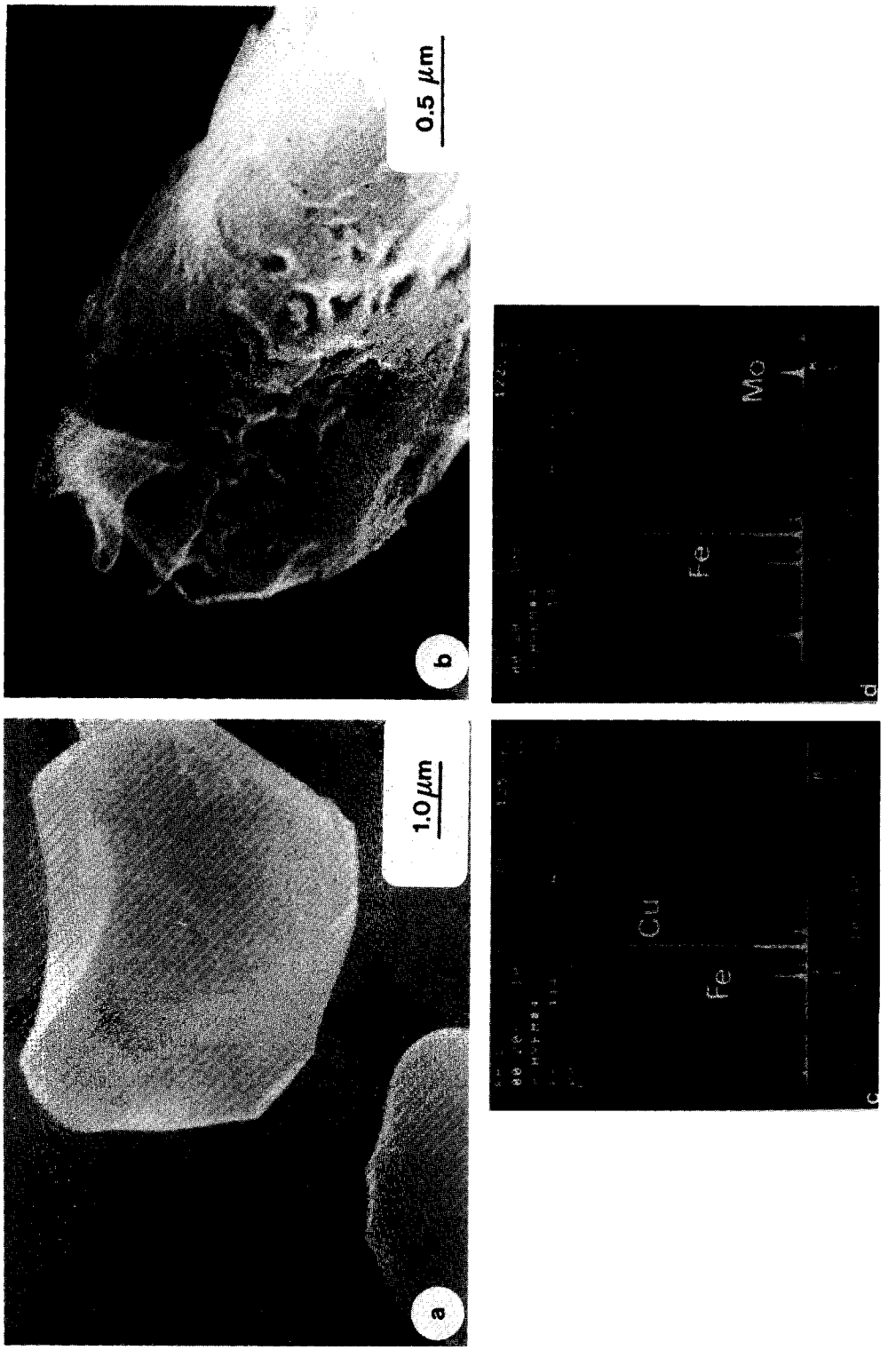

FIG. 2. SEM micrographs showing surface topography of (a) fresh $Fe_2Mo_3O_{12}$ catalyst particle, and (b) catalyst particle after reduction in 100 Torr CH_3OH/He environment at ~300°C showing surface roughness; (c) and (d) illustrate EDX spectra taken from the thin surface layer marked with small letter c in the image in (b) and from the bulk particle in (b), respectively. (Copper peak is from microscope grid.)

pled to an on-line image analysis (Intellect) system (*9*) for digital image processing. The microchemistry (local chemical composition) of the thin crystallites before and after the reactions was obtained using a Philips 400T analytical EM (AEM) and by EPMA (electron probe microanalysis) using an automated Cameca microprobe fitted with energy- and wavelength-dispersive spectrometers (EDS and WDS) (*10*).

RESULTS AND DISCUSSION

A. Ferric Molybdate ($Fe_2Mo_3O_{12}$)

An accurate analysis of the structural aspects of the catalytic material is required before its catalytic behavior can be correlated with its microstructure and nonstoichiometry. HREM is used to elucidate the microstructure. HREM images of $Fe_2Mo_3O_{12}$ (with lattice constants, a = 15.7 Å, b = 9.23 Å, c = 18.20 Å, and β = 125.1°, space group $P2_1/a$, and Z = 4; Ref. (*11*)) are shown in Figs. 1a, e, and f in (010), (101), and (121) projections, respectively, and these are likely faces exposed for catalysis. Figures 1b and c are digitally processed images of Fig. 1a using the on-line Intellect image-analysis facility (*9*) illustrating 15.7 Å layers. (Note the amorphous region near the edge of the crystal. Such regions may have implications in catalysis if genuinely associated with catalyst surfaces.) The electron diffraction pattern in (010) projection and the morphology of the fresh catalyst powder sample are shown as insets in Figs. 1d and f, respectively. Calculated images using the normal multislice methods (using the crystal structure data in Ref. (*11*)) are also inset in Figs. 1e and f, respectively. Calculated structures of $Fe_2Mo_3O_{12}$ in (010) projection are shown in Fig. 1g.

The fresh catalyst consists of defect-free single crystals of the order of a few micrometers in size as shown in the SEM image in Fig. 2a. TEM images also showed the fresh catalysts to be defect-free single crystallites. After reaction in reducing atmospheres (H_2 as well as MeOH) the ferric molybdate was observed to decompose into aggregates of microcrystals of either β-$FeMoO_4$ or α-Fe_2O_3 or a spinel structure as confirmed by a combination of electron diffraction, microdiffraction, and microanalysis. Figure 2b, for example, shows a reacted crystallite with considerable surface roughness. Note also a thin sheet of material (marked with small c) on the surface of the large particle. EDX analysis (illustrated in Fig. 2c) indicated that it contained only Fe, implying the existence of either a Fe oxide or, if completely reduced, metallic Fe. Analysis of the larger particle (marked with small d) indicated that it remained $Fe_2Mo_3O_{12}$ (Fig. 2d). In the *in situ* reactions in 10% H_2/He and alternatively in MeOH/He and MeOH/O_2 environments, at temperatures of ≥300°C, the ferric molybdate was observed to decompose into aggregates of either β-$FeMoO_4$, α-Fe_2O_3, or into a spinel structure. Evidence for these was contained in numerous electron diffraction patterns and images obtained during the *in situ* studies together with microstructural examinations of the reacted samples in the JEM 200CX HREM.

Figures 3a–d illustrate the sequence of an *in situ* reduction reaction; (a) fresh catalyst crystallite at room temperature (R.T.), near (010) projection, (b) corresponding electron diffraction pattern, with some forbidden reflections, (c) the sample after the reaction, showing precipitates, and (d) corresponding diffraction pattern (d.p.), showing β-$FeMoO_4$ rings. The diffraction pattern and images obtained in all the three environments suggested that reduction of $Fe_2Mo_3O_{12}$ proceeds via two or possibly three *simultaneous* routes. The first path involves reduction to β-$FeMoO_4$, the second appears to be via α-Fe_2O_3 (or $FeMoO_3$) and/or spinel (Fe_2MoO_4/Fe_3O_4), before reducing to metallic iron. The diffraction patterns and images in Figs. 4, 5, and 6 clearly illustrate these reaction paths. Figure 4a shows β-$FeMoO_4$ rings superimposed on a single-crystal ferric molybdate pattern; the high-resolution imaging of the reduced species confirmed the presence of $(\bar{1}31)$ β-$FeMoO_4$ crystallites as shown in Fig. 4b. Figures 5a–d illustrate

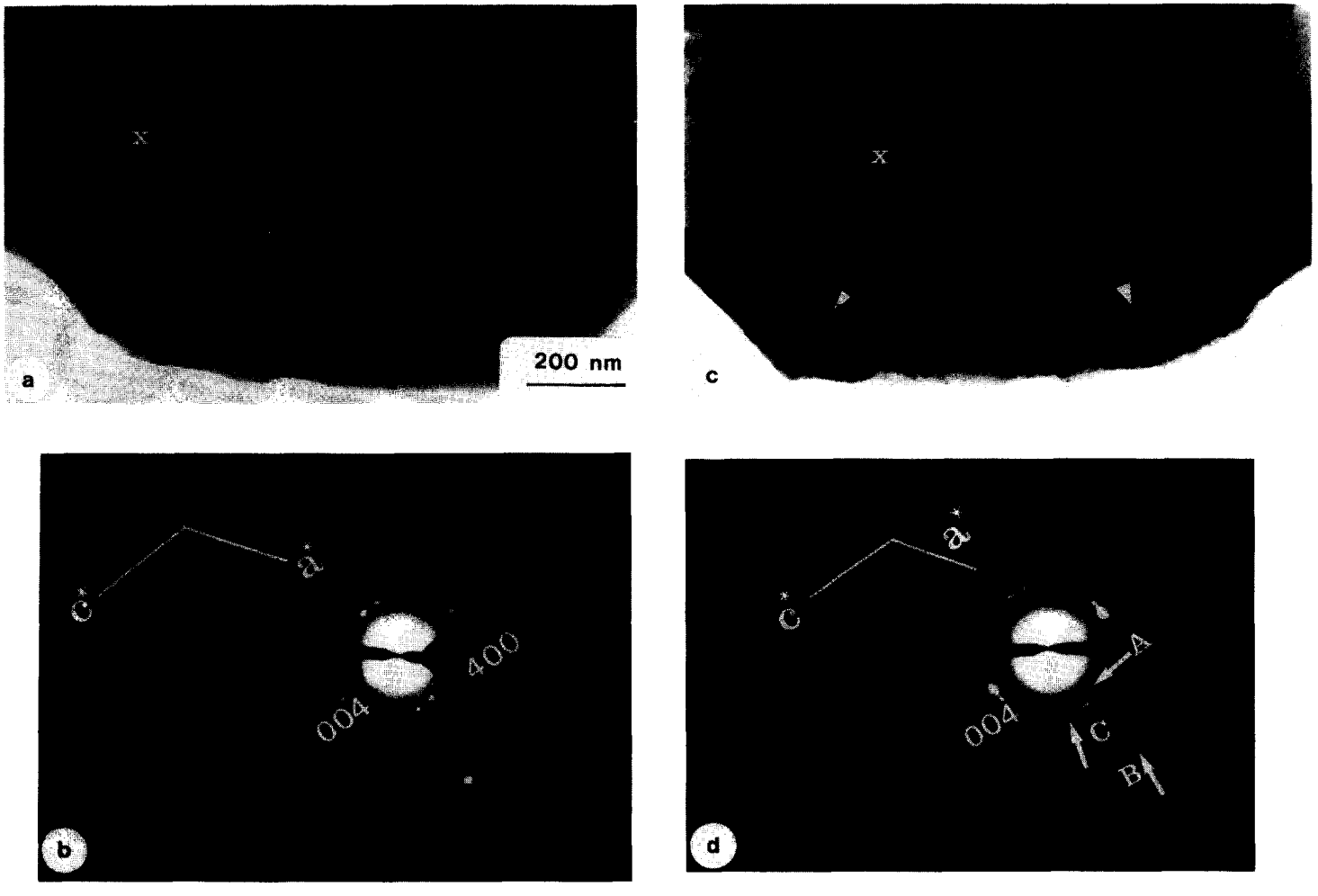

FIG. 3. Sequence of *in situ* reaction of $Fe_2Mo_3O_{12}$ in methanol/He. (a) Fresh ferric molybdate catalyst at room temperature; (b) corresponding diffraction pattern close to (010) orientation showing some low-index forbidden reflections (the crystallographic axes and some of the reflections are indexed); (c) the sample after the reaction at ~300°C showing precipitates; (d) corresponding selected-area diffraction pattern from the area with precipitates indicating β-$FeMoO_4$ rings superimposed on the host pattern (e.g., 004 reflection from the host material). The rings/spots in (d) due to $FeMoO_4$ at, e.g., A, C, and B are for 200, 111, and 222 reflections. (β-$FeMoO_4$ is monoclinic with a = 10.29 Å, b = 9.394 Å, c = 7.07 Å, β = 106.31°.)

the presence of α-Fe_2O_3 in the reduced material; (a) fibers of α-Fe_2O_3 formed during the reaction, (b) corresponding selected-area diffraction pattern showing $\langle 11\bar{2}0\rangle\alpha$-$Fe_2O_3$ reflections along with weak (diffuse) ferric molybdate reflections, (c) the fibers at higher magnification, and (d) microdiffraction and (e) microanalysis from one of the fibers confirming the presence of α-Fe_2O_3. Figure 6 shows spinel/rhombohedral microcrystalline species occurring in the reduction of the ferric molybdate: Fig. 6a shows microcrystals of the species and Fig. 6b illustrates the selected-area electron diffraction pattern from the crystal indicating the presence of rhombohedral and spinel species. Microchemical analyses of the reduced species provided further confirmation of these observations. Under somewhat severe reducing conditions (e.g.,

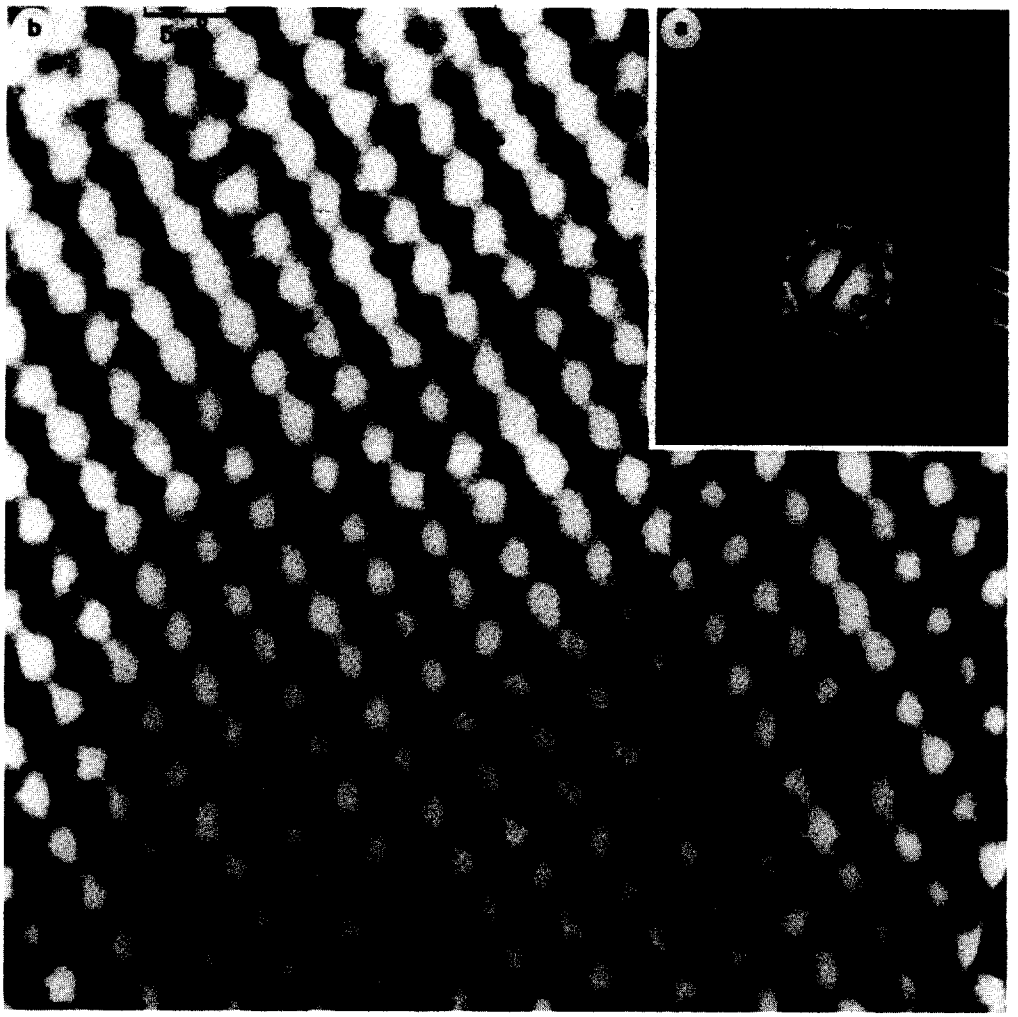

FIG. 4. (a) Electron diffraction pattern with β-$FeMoO_4$ rings superimposed on single-crystal ferric molybdate pattern shown, for example, by rows of arrows. The crystallographic axes and some reflections of the single crystal are illustrated; the ferric molybdate axes and 001 and 200 reflections are marked for reference. Rings of β-$FeMoO_4$ are shown, e.g., at A and B and correspond to $\bar{0}01$ and 111 reflections. (b) High-resolution lattice image of β-$FeMoO_4$ (from the reduced species) in $(\bar{1}31)$ projection with the computed image inset.

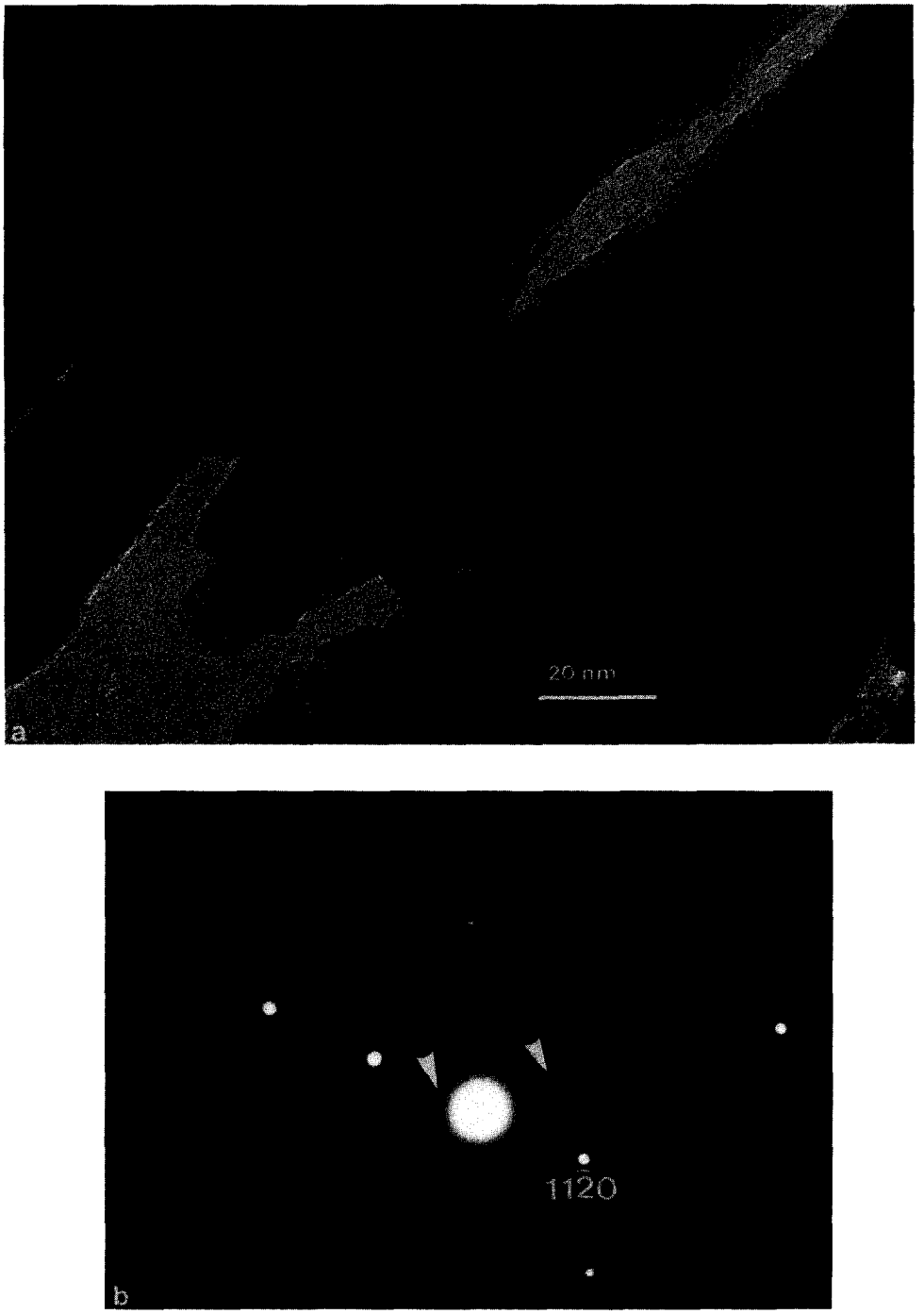

FIG. 5. (a) Fibers of α-Fe_2O_3 formed during reaction of ferric molybdate in MeOH–He. (b) Corresponding selected-area diffraction pattern showing $\langle 11\bar{2}0\rangle\alpha$-$Fe_2O_3$ reflections together with weak (diffuse) ferric molybdate reflections.

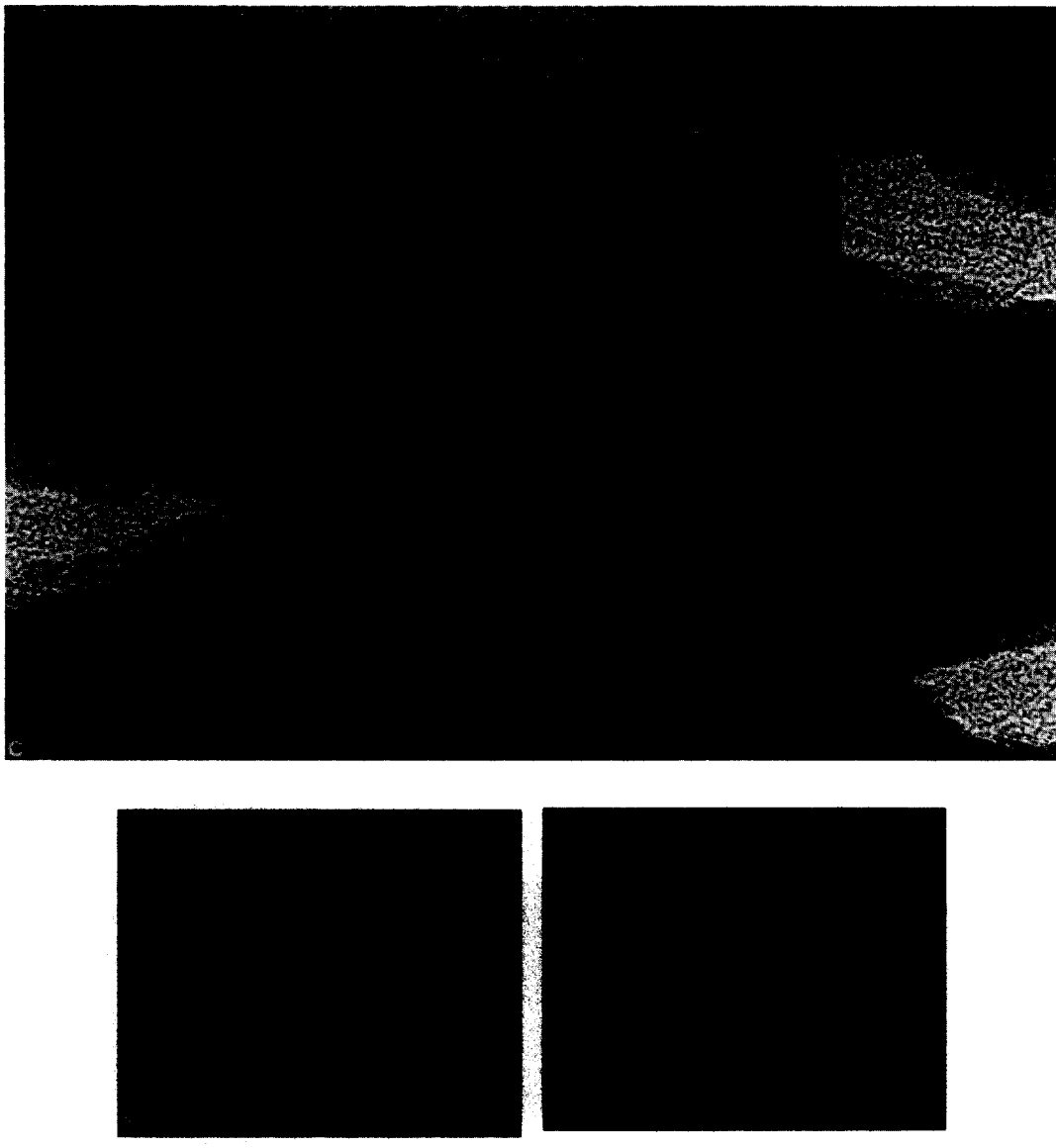

(c) α-Fe_2O_3 fibers at higher magnification (HREM image). (d) Microdiffraction. (e) Microanalysis (EDX) from one of the fibers shown in (a), confirming the presence of α-Fe_2O_3. (α-Fe_2O_3, rhombohedral, with a_{hex} = 5.04 Å and c_{hex} = 13.772 Å.)

in H_2/He or CH_3OH/He environments at 100 Torr pressure with temperatures ≥400°C) evidence for microcrystalline aggregates of α-Fe as well as γ-Fe was obtained. Electron diffraction patterns in Fig. 7 show the presence of α-Fe in the reacted material (suggesting segregation of iron) and β-$FeMoO_4$ with an orientation relationship $[1\bar{1}0]_\beta \parallel [001]_{\alpha\text{-Fe}}$. Figures 8a and b illustrate the HREM image of a γ-Fe crystallite and the corresponding diffraction pattern, respectively.

Parallel GC–MS experiments on the ferric molybdate in MeOH/He showed the formation of HCHO and H_2O. However, the selectivity to HCHO decreased significantly in the presence of the reduced species in the catalyst, indicating the active

phase to be $Fe_2Mo_3O_{12}$ for conversion of MeOH. Samples turned black after several hours, with CO and CO_2 being produced, and those samples examined by electron microscopy revealed carbon/graphite fibers. Carbon deposition coupled with loss of lattice oxygen may also suggest formation of some formic acid.

In $MeOH/O_2$ at a temperature ~300°C decomposition of the ferric molybdate was inhibited for up to several days with limited reduction to the phases/species described above (as observed in the dynamic EM), thus prolonging activity. Coking was also substantially reduced in the presence of oxygen gas.

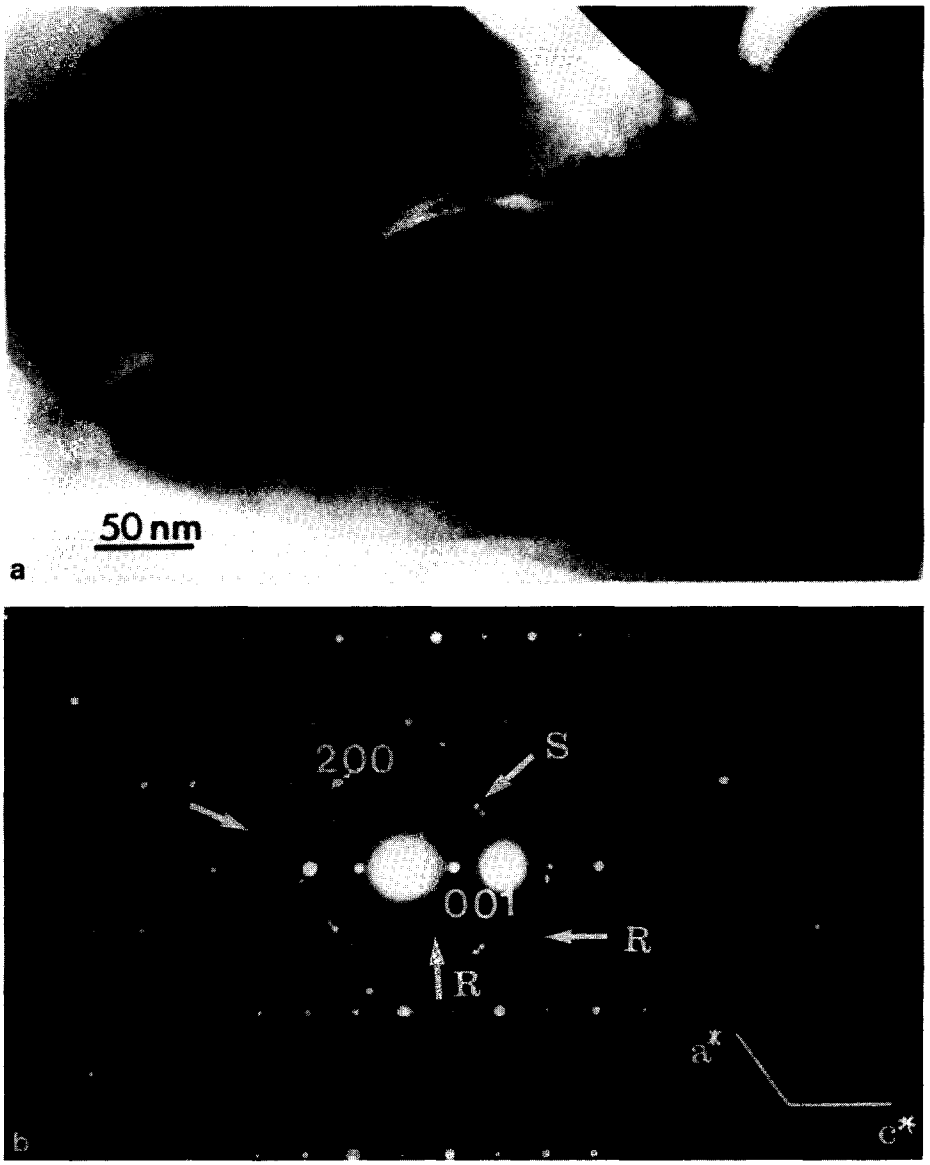

FIG. 6. (a) Microstructure of the reduced species (following reaction of ferric molybdate in MeOH); (b) electron diffraction pattern from the area in (a) indicating the presence of the spinel/rhombohedral species (arrowed). Rings/spots at S are for the spinel (e.g., Fe_3O_4) species and at R are for the 001 and 100 reflections of the rhombohedral α-Fe_2O_3 species.

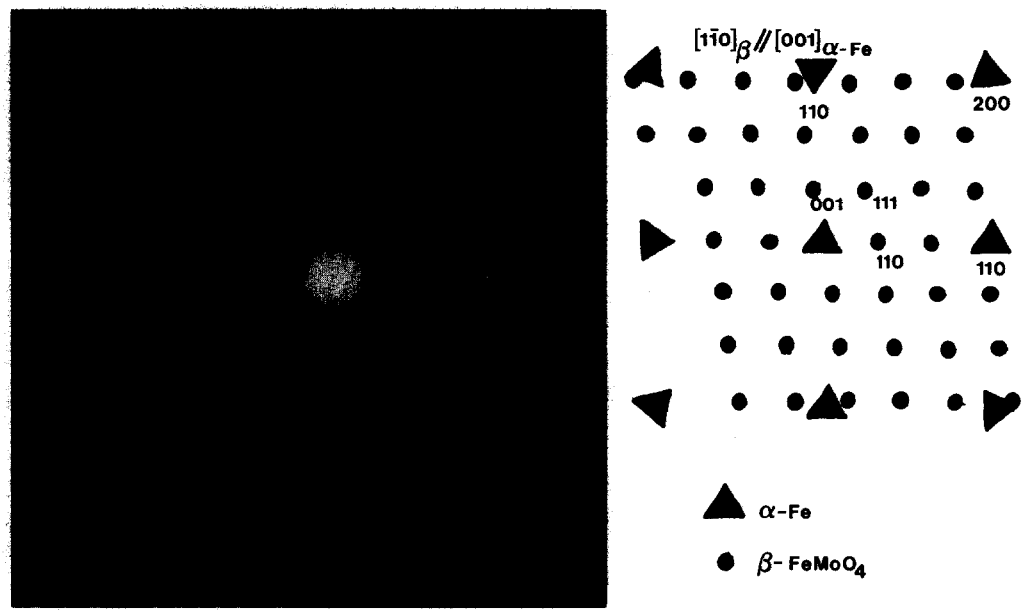

FIG. 7. Electron diffraction pattern showing orientation relationship $[1\bar{1}0]_{\beta\text{-}FeMoO_4} \parallel [001]_{\alpha\text{-}Fe}$.

From the *in situ* observations of microstructural changes of the ferric molybdate in MeOH (and also in H_2), it can be seen that the reduction proceeds via two or three routes simultaneously, namely via β-$FeMoO_4$ and α-Fe_2O_3 (and/or a spinel (Fe_2MoO_4/Fe_3O_4)).

B. MoO_3

In situ experiments have been repeated with (010) MoO_3 crystallites in the environments of H_2/He, methanol/He, and MeOH/O_2. The morphology of the crystallites is shown in Fig. 9. Increasing the temperature from R.T. (room temperature) to ~100°C in 10% H_2–He atmosphere, resulted in the formation of misfit dislocations in ~30 s, as shown in Fig. 10a. The defects are shown to be partial screw dislocations accommodating the misfit between the reduced surface layer and the underlying matrix (*12*). The sequence of reduction of MoO_3 in the H_2–He environment is shown in Figs. 10a–e. Figure 10b shows the nucleation of "surface platelets" or "domains" at ~120°C. The domains grow at higher temperatures as illustrated in Figs. 10c, s, and d. Detailed analysis of the defect structures is given in Refs. (*6*, *17*). Similar microstructural changes were observed in high-purity CO as well as in C_3H_6 environments.

In the MeOH/He environment, increasing the sample temperature from R.T. to ~100°C and keeping the sample at that temperature for several minutes showed no misfit dislocations of the type observed in H_2/He (shown in Fig. 10a). Increasing the temperature to ~250°C in MeOH/He resulted in the formation of a "domain" (platelet or twin) structure as shown in Fig. 11a (similar to the one observed in H_2/He). The domains grew by further reduction and the structure persisted up to ~350°C. The corresponding diffraction patterns exhibited an ordered superlattice (Fig. 11b) with two twin-related orientations of the domain structure contributing to the superlattice. The 101- and 301-type reflections gave weak diffracted intensity for the domains suggesting that they were probably extinguished in the domain structure.

The observations of domain growth by further reduction (Fig. 11c) or decomposition of MoO_3 *in vacuo* suggest that the do-

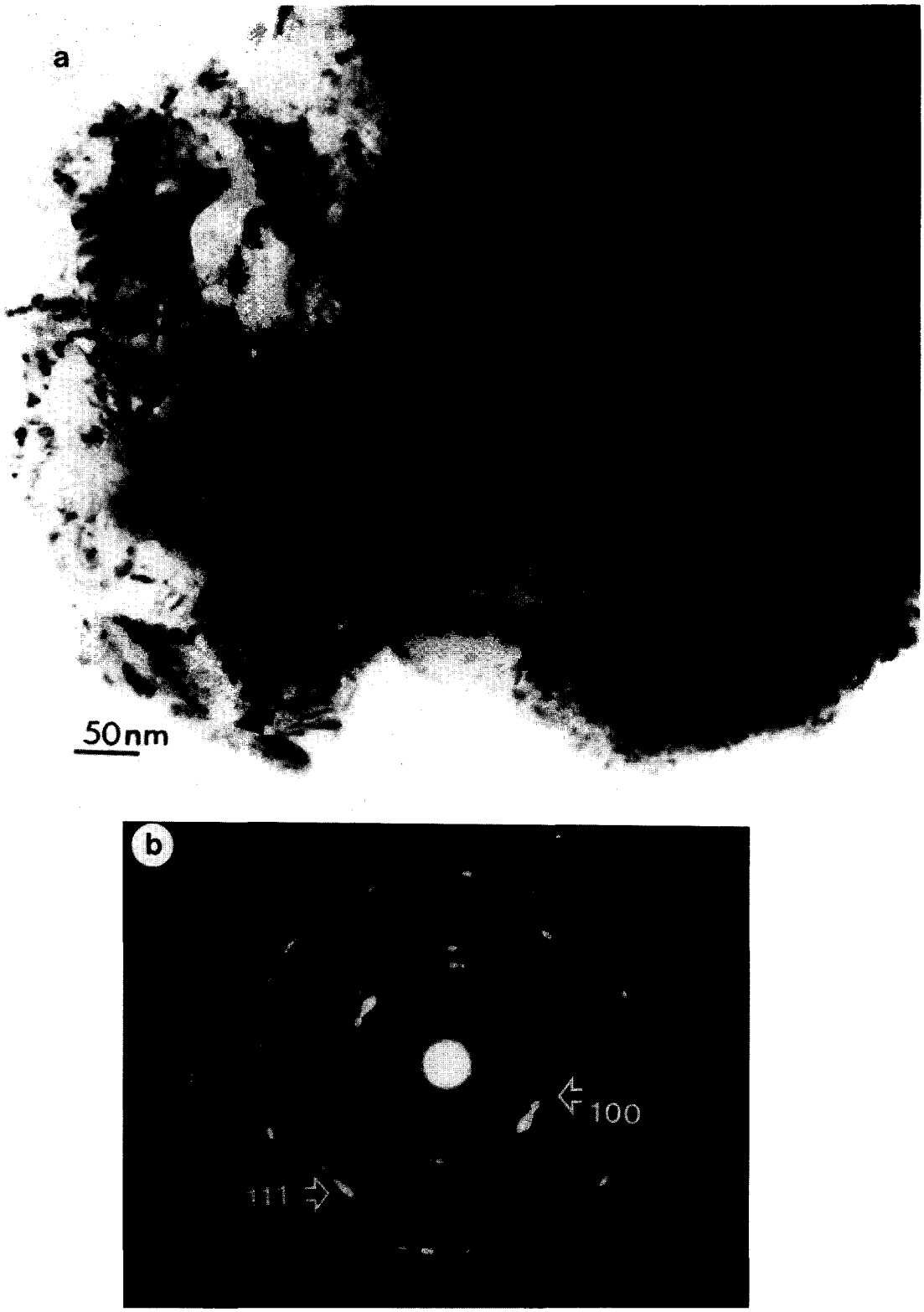

FIG. 8. (a) HREM image of γ-Fe crystallites obtained in the reduction of ferric molybdate in MeOH, and (b) corresponding electron diffraction pattern.

mains are oxygen deficient. An ordered array of oxygen vacancies gives rise to the correct extinction (and structure amplitudes) for the observed superlattice. The domains are thus thought to be regions of ordered anion vacancies, and that anion vacancy diffusion is essential for their formation.

The superlattice spacings deduced from the diffraction patterns are $\sim(7a \times 7c)_{MoO_3}$. Although tilting the crystal in the electron microscope has not provided sufficient information about the habit planes of the domains, the lattice spacings and contraction and expansion along the *a* and *c* directions suggest that the domain structure is perhaps close to the $Mo_{18}O_{52}$-type structure, which basically has a MoO_3 structure, i.e., MoO_3 provides the basic structure in this oxide (*13*). Thus, the basic structure forms slabs infinite in two dimensions and with a finite and characteristic width. These slabs are connected by edge-sharing between component octahedra in the neighboring slabs at the slab boundaries, forming a layer structure. The deficiency in oxygen compared to the host structure may be brought about by vacancy ordering. However, formation of hydroxides with similar lattice parameters (those of the type $Mo_4O_{10}(OH)_2$) may be possible in the MeOH and H_2 environments, where H_2O is one of the products (*15*). Some processes for methanol oxidation employ $MeOH/H_2O$ mixtures to

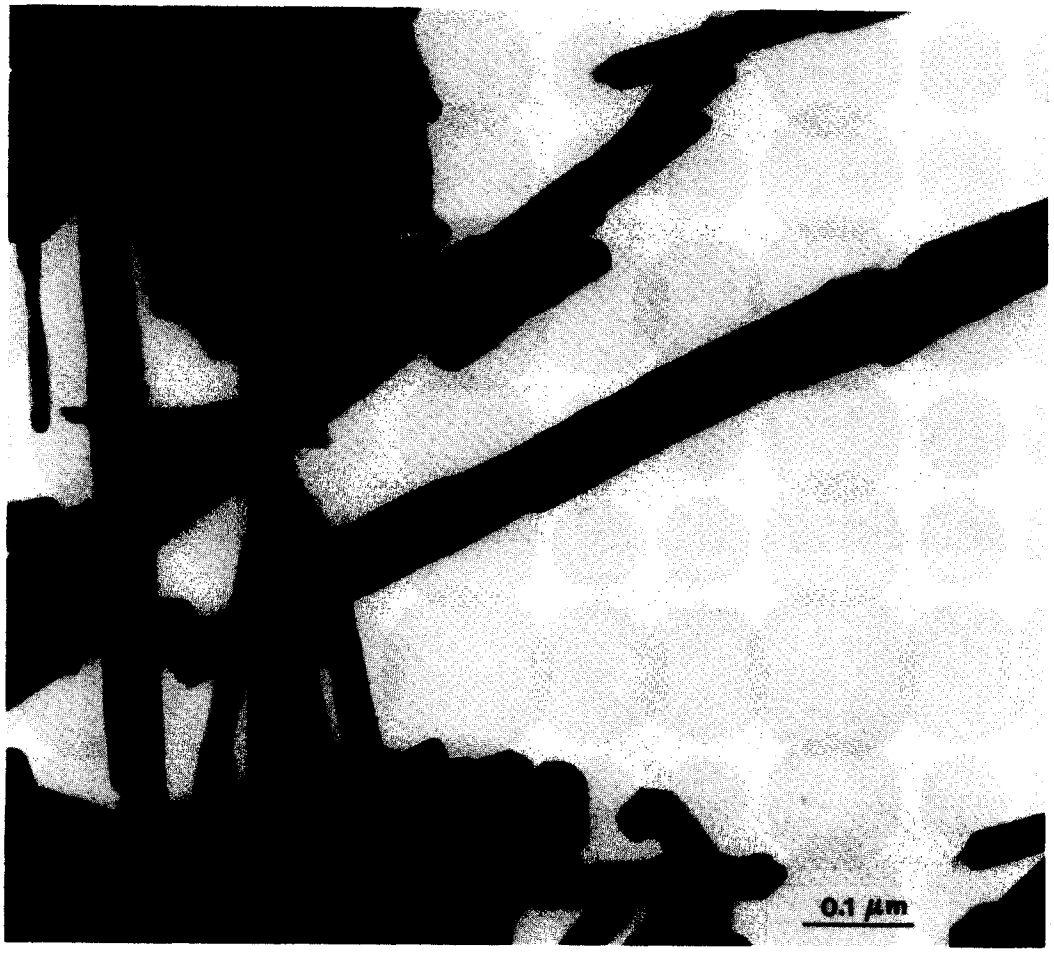

FIG. 9. Morphology of MoO_3 crystals. Most platelets have (010) habit.

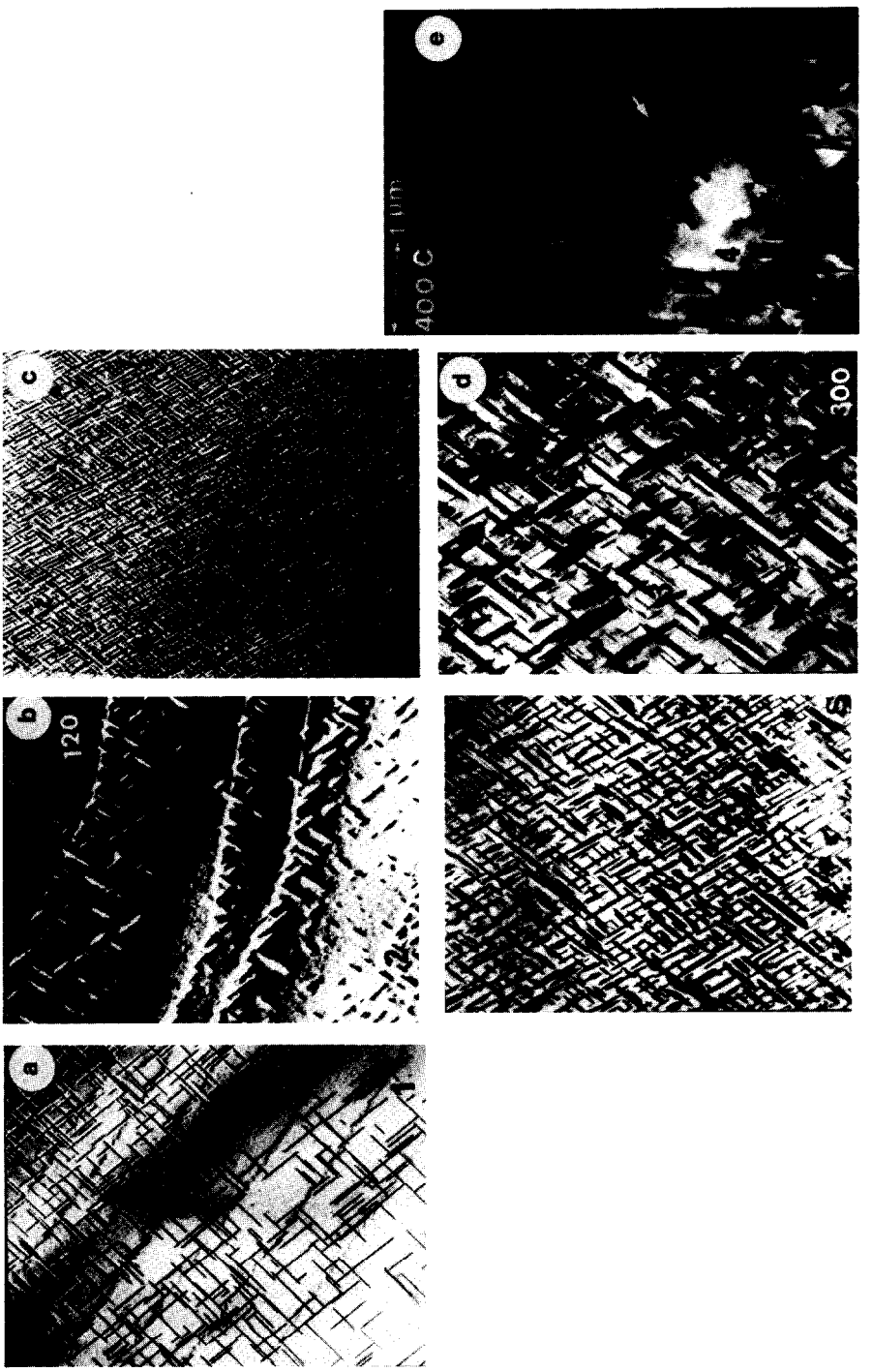

FIG. 10. Sequence of reduction of (010) MoO_3 in H_2 (balanced by He) environment. (a) Misfit dislocations observed at ~100°C. (b) "Surface platelets" or surface domains at 120°C. (c,s,d) Growth of domains at 170, 220, and 300°C. (e) Crystallographic shear planes at ~400°C.

enhance selectivity. Although H_2O inhibits the rate of reaction, it helps rapid desorption of HCHO. In the present experiments, at temperatures ≥300°C, the formation of molybdenum hydroxides is thought to be unlikely or difficult to ascertain, since identical domain (defect) structures were observed in high-purity carbon monoxide gas. Surface hydroxides may exist, but in general hydroxides are unstable above ~200°C. The domain structure in the experiments described existed up to ~350°C. The situation is further complicated by the fact that $Mo_{18}O_{52}$-type structures and $MoO_{2.5}(OH)_{0.5}$ have very similar lattice parameters (*13–15*).

At ≥380°C crystallographic shear (*CS*) planes were observed as shown in Fig. 11d of the sequence. These are produced parallel to the [001] direction and the black–white contrast shows that these are nucleated at crystal surfaces, as confirmed by stereomicroscopy and dynamical calculations. (The same defects were observed in the H_2–He mixture as shown in Fig. 10e.) The experiments suggested no diffraction contrast in 002 reflection, indicating edge-type dislocations (with collapse of the lat-

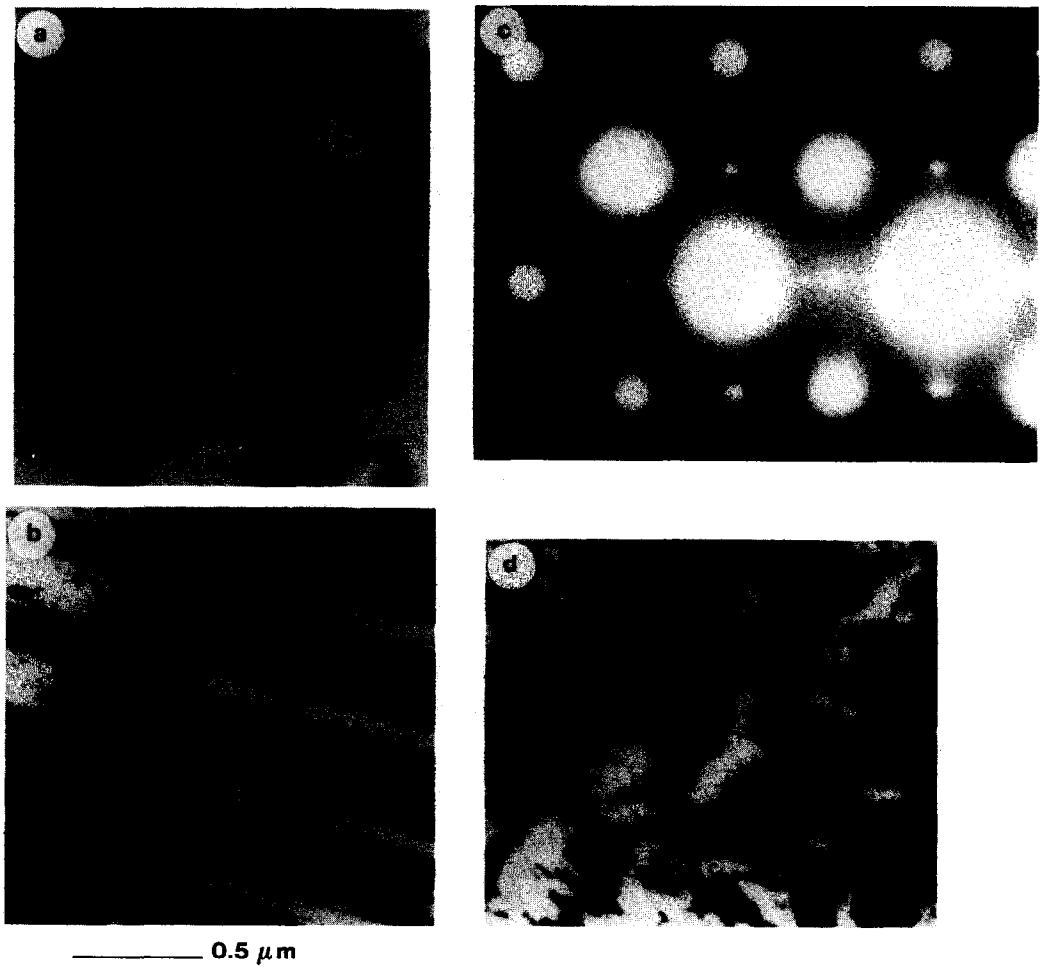

FIG. 11. Sequence of reduction of (010) MoO_3 in MeOH/He environment. (a) Domains at ~250°C and (b) their growth. (c) Corresponding electron diffraction pattern showing an ordered superlattice (indicated by arrows) around the main Bragg reflections. (d) Crystallographic shear planes at ≈400°C.

tice) and confirming crystallographic shear. The *CS* planes thus eliminate vacant oxygen sites (created by loss of lattice oxygen for catalysis) with a configuration $\langle a/2\ b/7\ 0\rangle$ {120}. [For details of the analysis, see Refs. (*6*, *17*).] The studies on nucleation and growth of these defects have confirmed the Anderson–Hyde model (*18*) of collapsed vacancy disks climbing by their bounding dislocation loop and the *CS* planes act as vacancy sinks. At ~400°C *CS* planes were present throughout the samples. Figure 11c shows that some small domains and misfit defects are also visible in the background. The samples disintegrated at temperatures ≥580°C in reduction and the corresponding ring electron diffraction patterns could be indexed as Mo_4O_{11}.

The observations in methanol/He suggest that the density of defects is much smaller than that in H_2/He environment. The reason for this and the implications for catalysis are not obvious at the present time.

Experiments on MoO_3 using $MeOH/O_2$ were carried out both *in situ* and using the GC–MS system from R.T. to ~400°C. No

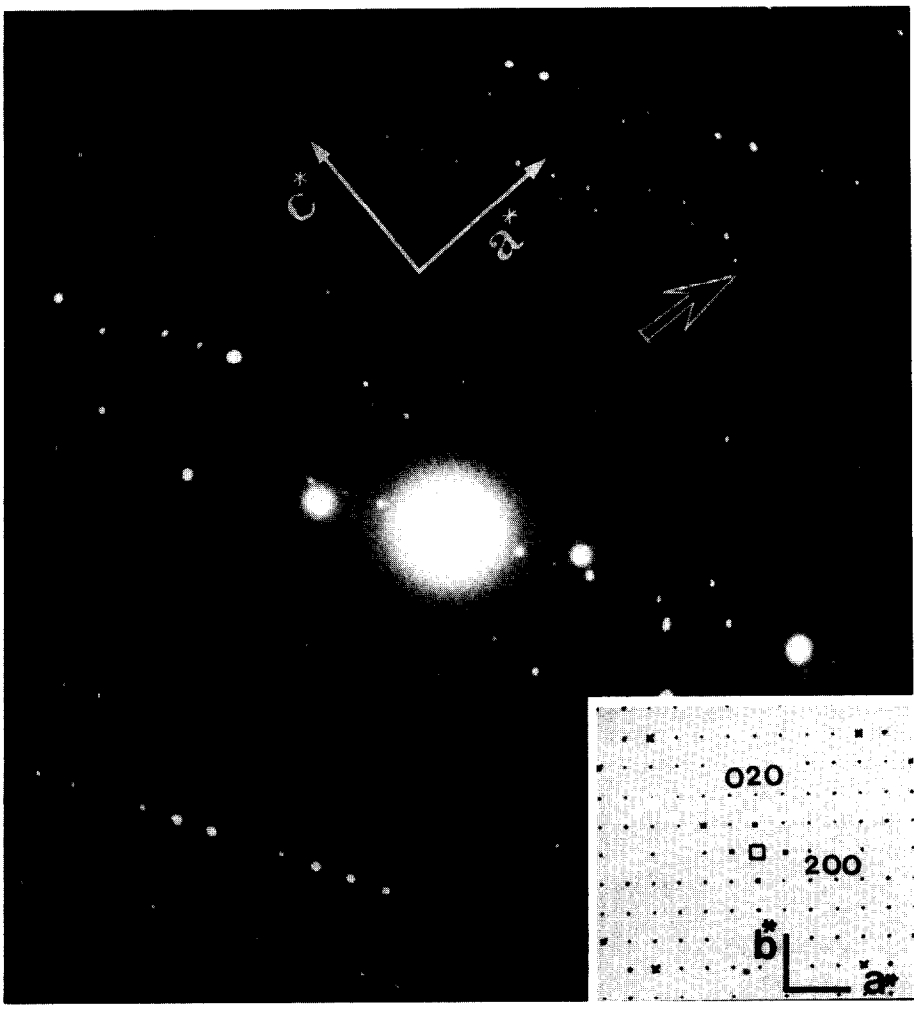

FIG. 12. Superlattice pattern obtained in experiments with MoO_3/MeOH, indexed as (001) $Mo_{17}O_{47}$ (indicated, e.g., by arrows). The inset shows a schematic diagram of the superlattice. The host (010) MoO_3 axes are indicated and the $(101)_{MoO_3}$ reflections are shown by A and B.

significant changes in defect morphology were observed below ~250°C and (010) MoO_3 was found to be not much active for methanol oxidation. Even in the presence of gaseous oxygen, domain structures (as described earlier) characteristic of reduction were observed. Noticeable changes occurred from ~300°C and *CS* planes were observed to reoxidize at ≥380°C. The presence of suboxides was also observed in the samples reacted in the mixture for longer periods (days) as shown in the example in Fig. 12. The superlattice pattern (superimposed on the host pattern, B) is indexed as (001) $Mo_{17}O_{47}$ structure. Confirmation of this in other crystallographic zones was not possible due to the limited tilt range available in the HVEM. Some crystallites with Mo_4O_{11} structure were also present. The observations indicate that many consecutive and complex reactions occur simultaneously when the catalyst samples are kept under reaction conditions for long periods.

In situ experiments carried out on iron–molybdate–MoO_3 physical mixtures in MeOH/He between 200 and 400°C showed that they remain as distinct phases, with the same microstructural changes as above.

CONCLUSIONS

The dynamic experiments coupled with parallel chemical studies have shown that reduction of $Fe_2Mo_3O_{12}$ catalyst in methanol or H_2 environments proceeds via two or three routes simultaneously, with production of ferrous molybdate, α-Fe_2O_3 and/or spinel phases, and eventually metallic Fe. In the presence of gaseous oxygen reduction occurs to a limited extent and selectivity and activity of the catalyst are prolonged. Electron microscopy and GC–MS experiments described in the preceding paragraphs suggest that the mechanism of methanol oxidation involves the release of lattice oxygen. Various suggestions have been made regarding the role of Fe and Mo ions and the rate-determining step in the selective oxidation of methanol (*1, 2, 4*). Machiels and Sleight (*3*) have confirmed that the initial chemisorption of methanol is dissociative, forming surface methoxy groups, and have shown that the rate-determining step on MoO_3 and ferric molybdate is the breaking of a carbon–hydrogen bond to form adsorbed formaldehyde and that Fe acts as a stabilizer in the reactions. *In situ* electron microscopy experiments carried out on MoO_3 in H_2/He and in methanol/He have shown that identical defect structures are obtained in both the environments above 200°C but the density of the defects is lower in MeOH/He.

ACKNOWLEDGMENTS

We would like to thank the SERC (U.K.) for support, Professor Sir Peter Hirsch for the provision of laboratory facilities, Dr. A. W. Sleight and colleagues at DuPont Central Research and Development Department, Delaware, for very useful discussions, and the National Science Foundation (USA)/NATO for a fellowship grant (P.A.L.) at Oxford.

REFERENCES

1. Jírů, P., Wichterlova, B., and Tichy, J., "Proceedings, 3rd International Congress on Catalysis, (Amsterdam, 1964)," Vol. 1, p. 199. North-Holland, Amsterdam, 1965.
2. Pernicone, N., *J. Less-Common Met.* **36,** 289 (1974).
3. Machiels, C. J., and Sleight, A. W., *J. Catal.* **76,** 238 (1982).
4. Popov, B. I., Osipova, K. D., and Pan Krater, Y. D., *Kinet. Catal.* **12,** 1102 (1971).
5. Machiels, C. J., and Sleight, A. W., *in* "Proceedings, 4th International Conference on Molybdenum Chemistry" (H. F. Barry and P. C. H. Mitchell, Eds.), p. 411, Climax Molybdenum Co., Michigan, 1982.
6. Gai, P. L., *Philos. Mag.* **43,** 841 (1981).
7. Swann, P. R., and Tighe, N., *Jernkontorets Ann.* **155,** 479 (1971).
8. Boyes, E. D., Watanabe, E., Skarnulis, A. J., Hutchison, J. L., Gai, P. L., Jenkins, M. L., and Naruse, M., in "Proceedings, EMAG 79, Inst. Physics (London), Conf. Ser.," Vol. 52, p. 445, 1980.
9. Boyes, E. D., Muggridge, B., and Goringe, M. J., *J. Microsc.* **127,** 321 (1982).
10. Gai, P. L., *J. Solid State Chem.* **49,** 25 (1983).
11. Chen, H., *Mater. Res. Bull.* **21,** 19 (1979).
12. Thoeni, W., Gai, P. L., and Hirsch, P. B., *J. Less-Common Met.* **54,** 263 (1977).

13. Kihlborg, L., *Ark. Kemi* **21,** 471 (1963).
14. Dowell, W. C. T., Bursill, L. A., Goodman, P., and Tate, N., *Acta Crystallogr. Sect. A* **34,** 296 (1974).
15. Glemser, O., and Lutz, P., *Z. Anorg. Allg. Chem.* **264,** 17 (1951).
16. Schollhörn, R., Kuhlmann, R., and Besenhard, J. O., *Mater. Res. Bull.* **11,** 83 (1976).
17. Bursill, L. A., *Proc. R. Soc. London Ser. A* **311,** 267 (1963).
18. Anderson, J. S., and Hyde, B. G., *J. Phys. Chem. Solids* **28,** 1393 (1967).